Neural Sparse Voxel Fields

Lingjie Liu[†*]**, Jiatao Gu**[‡*]**, Kyaw Zaw Lin**[◇]**, Tat-Seng Chua**[◇]**, Christian Theobalt**[†]
[†]Max Planck Institute for Informatics
[‡]Facebook AI Research   [◇]National University of Singapore
[†]{lliu,theobalt}@mpi-inf.mpg.de
[‡]jgu@fb.com   [◇]kyawzl@comp.nus.edu.sg
[◇]dcscts@nus.edu.sg

Abstract

Photo-realistic free-viewpoint rendering of real-world scenes using classical computer graphics techniques is challenging, because it requires the difficult step of capturing detailed appearance and geometry models. Recent studies have demonstrated promising results by learning scene representations that implicitly encode both geometry and appearance without 3D supervision. However, existing approaches in practice often show blurry renderings caused by the limited network capacity or the difficulty in finding accurate intersections of camera rays with the scene geometry. Synthesizing high-resolution imagery from these representations often requires time-consuming optical ray marching. In this work, we introduce *Neural Sparse Voxel Fields (NSVF)*, a new neural scene representation for fast and high-quality free-viewpoint rendering. NSVF defines a set of voxel-bounded implicit fields organized in a sparse voxel octree to model local properties in each cell. We progressively learn the underlying voxel structures with a diffentiable ray-marching operation from only a set of posed RGB images. With the sparse voxel octree structure, rendering novel views can be accelerated by skipping the voxels containing no relevant scene content. Our method is typically over 10 times faster than the state-of-the-art (namely, NeRF (Mildenhall et al., 2020)) at inference time while achieving higher quality results. Furthermore, by utilizing an explicit sparse voxel representation, our method can easily be applied to scene editing and scene composition. We also demonstrate several challenging tasks, including multi-scene learning, free-viewpoint rendering of a moving human, and large-scale scene rendering. Code and data are available at our website: https://github.com/facebookresearch/NSVF.

1 Introduction

Realistic rendering in computer graphics has a wide range of applications including mixed reality, visual effects, visualization, and even training data generation in computer vision and robot navigation. Photo-realistically rendering a real world scene from arbitrary viewpoints is a tremendous challenge, because it is often infeasible to acquire high-quality scene geometry and material models, as done in high-budget visual effects productions. Researchers therefore have developed image-based rendering (IBR) approaches that combine vision-based scene geometry modeling with image-based view interpolation (Shum and Kang, 2000; Zhang and Chen, 2004; Szeliski, 2010). Despite their significant progress, IBR approaches still have sub-optimal rendering quality and limited control over the results, and are often scene-type specific. To overcome these limitations, recent works have employed deep neural networks to implicitly learn scene representations encapsulating both geometry and appearance from 2D observations with or without a coarse geometry. Such neural representations are commonly

---

[*]Equal contribution.

combined with 3D geometric models, such as voxel grids (Yan et al., 2016; Sitzmann et al., 2019a; Lombardi et al., 2019), textured meshes (Thies et al., 2019; Kim et al., 2018; Liu et al., 2019a, 2020), multi-plane images (Zhou et al., 2018; Flynn et al., 2019; Mildenhall et al., 2019), point clouds (Meshry et al., 2019; Aliev et al., 2019), and implicit functions (Sitzmann et al., 2019b; Mildenhall et al., 2020).

Unlike most explicit geometric representations, neural implicit functions are smooth, continuous, and can - in theory - achieve high spatial resolution. However, existing approaches in practice often show blurry renderings caused by the limited network capacity or the difficulty in finding accurate intersections of camera rays with the scene geometry. Synthesizing high-resolution imagery from these representations often requires time-consuming optical ray marching. Furthermore, editing or re-compositing 3D scene models with these neural representations is not straightforward.

In this paper, we propose *Neural Sparse Voxel Fields* (NSVF), a new implicit representation for fast and high-quality free-viewpoint rendering. Instead of modeling the entire space with a single implicit function, NSVF consists of a set of voxel-bounded implicit fields organized in a sparse voxel octree. Specifically, we assign a voxel embedding at each vertex of the voxel, and obtain the representation of a query point inside the voxel by aggregating the voxel embeddings at the eight vertices of the corresponding voxel. This is further passed through a multilayer perceptron network (MLP) to predict geometry and appearance of that query point. Our method can progressively learn NSVF from coarse to fine with a differentiable ray-marching operation from only a set of posed 2D images of a scene. During training, the sparse voxels containing no scene information will be pruned to allow the network to focus on the implicit functions learning for volume regions with scene contents. With the sparse voxels, rendering at inference time can be greatly accelerated by skipping empty voxels without scene content.

Our method is typically over 10 times faster than the state-of-the-art (namely, NeRF (Mildenhall et al., 2020)) at inference time while achieving higher quality results. We extensively evaluate our method on a variety of challenging tasks including multi-object learning, free-viewpoint rendering of dynamic and indoor scenes. Our method can be used to edit and composite scenes. To summarize, our technical contributions are:

- We present NSVF that consists of a set of voxel-bounded implicit fields, where for each voxel, voxel embeddings are learned to encode local properties for high-quality rendering;

- NSVF utilizes the sparse voxel structure to achieve efficient rendering;

- We introduce a progressive training strategy that efficiently learns the underlying sparse voxel structure with a differentiable ray-marching operation from a set of posed 2D images in an end-to-end manner.

2 Background

Existing neural scene representations and neural rendering methods commonly aim to learn a function that maps a spatial location to a feature representation that implicitly describes the local geometry and appearance of the scene, where novel views of that scene can be synthesized using rendering techniques in computer graphics. To this end, the rendering process is formulated in a differentiable way so that the neural network encoding the scene representation can be trained by minimizing the difference between the renderings and 2D images of the scene. In this section, we describe existing approaches to representation and rendering using implicit fields and their limitations.

2.1 Neural Rendering with Implicit Fields

Let us represent a scene as an implicit function $F_\theta \colon (\boldsymbol{p}, \boldsymbol{v}) \to (\boldsymbol{c}, \omega)$, where θ are parameters of an underlying neural network. This function describes the scene color $\boldsymbol{c}$ and its probability density ω at spatial location $\boldsymbol{p}$ and ray direction $\boldsymbol{v}$. Given a pin-hole camera at position $\boldsymbol{p}_0 \in \mathbb{R}^3$, we render a 2D image of size $H \times W$ by shooting rays from the camera to the 3D scene. We thus evaluate a volume rendering integral to compute the color of camera ray $\boldsymbol{p}(z) = \boldsymbol{p}_0 + z \cdot \boldsymbol{v}$ as:

$$\boldsymbol{C}(\boldsymbol{p}_0, \boldsymbol{v}) = \int_0^{+\infty} \omega(\boldsymbol{p}(z)) \cdot \boldsymbol{c}(\boldsymbol{p}(z), \boldsymbol{v}) dz, \quad \text{where} \int_0^{+\infty} \omega(\boldsymbol{p}(z)) dz = 1 \qquad (1)$$

Note that, to encourage the scene representation to be multiview consistent, ω is restricted as a function of only $\boldsymbol{p}(z)$ while $\boldsymbol{c}$ takes both $\boldsymbol{p}(z)$ and $\boldsymbol{v}$ as inputs to model view-dependent color. Different rendering strategies to evaluate this integral are feasible.

Surface Rendering. Surface-based methods (Sitzmann et al., 2019b; Liu et al., 2019b; Niemeyer et al., 2019) assume $\omega(\boldsymbol{p}(z))$ to be the Dirac function $\delta(\boldsymbol{p}(z) - \boldsymbol{p}(z^*))$ where $\boldsymbol{p}(z^*)$ is the intersection of the camera ray with the scene geometry.

Volume Rendering. Volume-based methods (Lombardi et al., 2019; Mildenhall et al., 2020) estimate the integral $\boldsymbol{C}(\boldsymbol{p}_0, \boldsymbol{v})$ in Eq. 1 by densely sampling points on each camera ray and accumulating the colors and densities of the sampled points into a 2D image. For example, the state-of-the-art method NeRF (Mildenhall et al., 2020) estimates $\boldsymbol{C}(\boldsymbol{p}_0, \boldsymbol{v})$ as:

$$\boldsymbol{C}(\boldsymbol{p}_0, \boldsymbol{v}) \approx \sum_{i=1}^{N} \left(\prod_{j=1}^{i-1} \alpha(z_j, \Delta_j) \right) \cdot (1 - \alpha(z_i, \Delta_i)) \cdot \boldsymbol{c}(\boldsymbol{p}(z_i), \boldsymbol{v}) \tag{2}$$

where $\alpha(z_i, \Delta_i) = \exp(-\sigma(\boldsymbol{p}(z_i) \cdot \Delta_i))$, and $\Delta_i = z_{i+1} - z_i$. $\{\boldsymbol{c}(\boldsymbol{p}(z_i), \boldsymbol{v})\}_{i=1}^{N}$ and $\{\sigma(\boldsymbol{p}(z_i))\}_{i=1}^{N}$ are the colors and the volume densities of the sampled points.

2.2 Limitations of Existing Methods

For surface rendering, it is critically important that an accurate surface is found for learned color to be multi-view consistent, which is hard and detrimental to training convergence so that induces blur in the renderings. Volume rendering methods need to sample a high number of points along the rays for color accumulation to achieve high quality rendering. However, evaluation of each sample points along the ray as NeRF does is inefficient. For instance, it takes around 30 seconds for NeRF to render an 800×800 image. Our main insight is that it is important to prevent sampling of points in empty space without relevant scene content as much as possible. Although NeRF performs importance sampling along the ray, due to allocating fixed computational budget for every ray, it cannot exploit this opportunity to improve rendering speed. We are inspired by classical computer graphics techniques such as the bounding volume hierarchy (BVH, Rubin and Whitted, 1980) and the sparse voxel octree (SVO, Laine and Karras, 2010) which are designed to model the scene in a sparse hierarchical structure for ray tracing acceleration. In this encoding, local properties of a spatial location only depend on a local neighborhood of the leaf node that the spatial location belongs to. In this paper we show how hierarchical sparse volume representations can be used in a neural network-encoded implicit field of a 3D scene to enable detailed encoding, and efficient, high quality differentiable volumetric rendering, even of large scale scenes.

3 Neural Sparse Voxel Fields

In this section, we introduce *Neural Sparse-Voxel Fields* (NSVF), a hybrid scene representation that combines neural implicit fields with an explicit sparse voxel structure. Instead of representing the entire scene as a single implicit field, NSVF consists of a set of voxel-bounded implicit fields organized in a sparse voxel octree. In the following, we describe the building block of NSVF - a voxel-bounded implicit field (§ 3.1) - followed by a rendering algorithm for NSVF (§ 3.2), and a progressive learning strategy (§ 3.3).

3.1 Voxel-bounded Implicit Fields

We assume that the relevant non-empty parts of a scene are contained within a set of sparse (bounding) voxels $\mathcal{V} = \{V_1 \ldots V_K\}$, and the scene is modeled as a set of voxel-bounded implicit functions: $F_\theta(\boldsymbol{p}, \boldsymbol{v}) = F_\theta^i(\boldsymbol{g}_i(\boldsymbol{p}), \boldsymbol{v})$ if $\boldsymbol{p} \in V_i$. Each F_θ^i is modeled as a multi-layer perceptron (MLP) with shared parameters θ:

$$F_\theta^i : (\boldsymbol{g}_i(\boldsymbol{p}), \boldsymbol{v}) \rightarrow (\boldsymbol{c}, \sigma), \forall \boldsymbol{p} \in V_i, \tag{3}$$

Here $\boldsymbol{c}$ and σ are the color and density of the 3D point $\boldsymbol{p}$, $\boldsymbol{v}$ is ray direction, $g_i(\boldsymbol{p})$ is the representation at $\boldsymbol{p}$ which is defined as:

$$g_i(\boldsymbol{p}) = \zeta \left(\chi \left(\widetilde{g}_i(\boldsymbol{p}_1^*), \ldots, \widetilde{g}_i(\boldsymbol{p}_8^*) \right) \right) \tag{4}$$
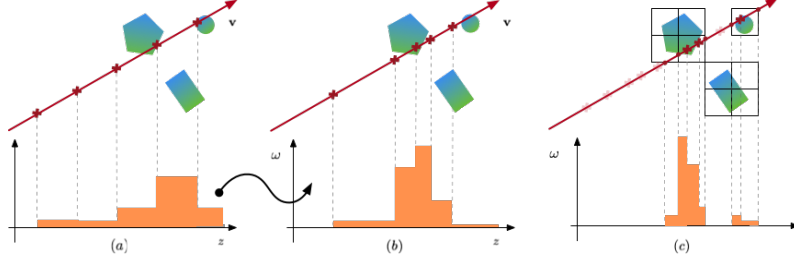
Figure 1: Illustrations of (a) uniform sampling; (b) importance sampling based on the results in (a); (c) the proposed sampling approach based on sparse voxels.

where $\boldsymbol{p}_1^*, \ldots, \boldsymbol{p}_8^* \in \mathbb{R}^3$ are the eight vertices of V_i, and $\widetilde{g}_i(\boldsymbol{p}_1^*), \ldots, \widetilde{g}_i(\boldsymbol{p}_8^*) \in \mathbb{R}^d$ are feature vectors stored at each vertex. In addition, $\chi(.)$ refers to trilinear interpolation, and $\zeta(.)$ is a post-processing function. In our experiments, $\zeta(.)$ is positional encoding proposed by (Vaswani et al., 2017; Mildenhall et al., 2020).

Compared to using the 3D coordinate of point $\boldsymbol{p}$ as input to F_θ^i as most of previous works do, in NSVF, the feature representation $g_i(\boldsymbol{p})$ is aggregated by the eight voxel embeddings of the corresponding voxel where region-specific information (e.g. geometry, materials, colors) can be embedded. It significantly eases the learning of subsequent F_θ^i as well as facilitates high-quality rendering.

Special Cases. NSVF subsumes two classes of earlier works as special cases. (1) When $\widetilde{g}_i(\boldsymbol{p}_k^*) = \boldsymbol{p}_k^*$ and $\zeta(.)$ is the positional encoding, $g_i(\boldsymbol{p}) = \zeta(\chi(\boldsymbol{p}_1^*, \ldots, \boldsymbol{p}_8^*)) = \zeta(\boldsymbol{p})$, which means that NeRF (Mildenhall et al., 2020) is a special case of NSVF. (2) When $\widetilde{g}_i(\boldsymbol{p}) : \boldsymbol{p} \to (\boldsymbol{c}, \sigma)$, $\zeta(.)$ and F_θ^i are identity functions, our model is equivalent to the models which use explicit voxels to store colors and densities, e.g., Neural Volumes (Lombardi et al., 2019).

3.2 Volume Rendering

NSVF encodes the color and density of a scene at any point $\boldsymbol{p} \in \mathcal{V}$. Compared to rendering a neural implicit representation that models the entire space, rendering NSVF is much more efficient as it obviates sampling points in the empty space. Rendering is performed in two steps: (1) ray-voxel intersection; and (2) ray-marching inside voxels. We illustrate the pipeline in Appendix Figure 8,

Ray-voxel Intersection. We first apply Axis Aligned Bounding Box intersection test (AABB-test) (Haines, 1989) for each ray. It checks whether a ray intersects with a voxel by comparing the distances from the ray origin to each of the six bounding planes of the voxel. The AABB test is very efficient especially for a hierarchical octree structure (e.g. NSVF), as it can readily process millions of voxels in real time. Our experiments show that $10k \sim 100k$ sparse voxels in the NSVF representation are enough for photo-realistic rendering of complex scenes.

Ray Marching inside Voxels. We return the color $\boldsymbol{C}(\boldsymbol{p}_0, \boldsymbol{v})$ by sampling points along a ray using Eq. (2). To handle the case where a ray misses all the objects, we additionally add a background term $A(\boldsymbol{p}_0, \boldsymbol{v}) \cdot \boldsymbol{c}_{\mathrm{bg}}$ on the right side of Eq. (2), where we define *transparency* $A(\boldsymbol{p}_0, \boldsymbol{v}) = \prod_{i=1}^N \alpha(z_i, \Delta_i)$, and $\boldsymbol{c}_{\mathrm{bg}}$ is learnable RGB values for background. As discussed in § 2, volume rendering requires dense samples along the ray in non-empty space to achieve high quality rendering. Densely evaluating at uniformly sampled points in the whole space (Figure 1 (a)) is inefficient because empty regions are frequently and unnecessarily tested. To focus on sampling in more important regions, Mildenhall et al. (2020) learned two networks where the second network is trained with samples from the distribution estimated by the first one (Figure 1 (b)). However, this further increases the training and inference complexity. In contrast, NSVF does not employ a secondary sampling stage while achieving better visual quality. As shown in Figure 1 (c), we create a set of query points using rejection sampling based on sparse voxels. Compared to the aforementioned approaches, we are able to sample more densely at the same evaluation cost. We include all voxel intersection points as additional samples and perform color accumulation with the *midpoint rule*. Our approach is summarized in Algorithm 1 where we additionally return the transparency A, and the expected depth Z which can be further used for visualizing the normal with finite difference.
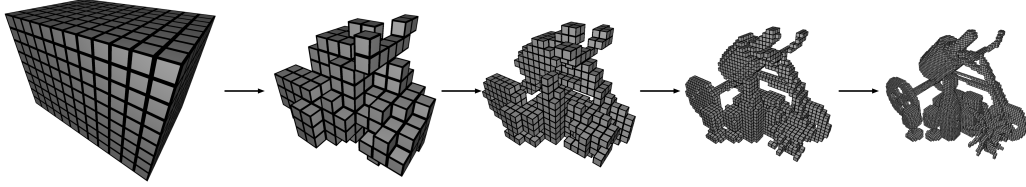
4

Figure 2: Illustration of self-pruning and progressive training

Early Termination. NSVF can represent transparent and solid objects equally well. However, for solid surfaces, the proposed volume rendering disperses the surface color along the ray, which means that it takes many unnecessary accumulation steps behind the surface to make the accumulated transparency $A(\boldsymbol{p}_0, \boldsymbol{v})$ reach 0. We therefore use a heuristic and stop evaluating points earlier when the accumulated transparency $A(\boldsymbol{p}_0, \boldsymbol{v})$ drops below a certain threshold ϵ. In our experiments, we find that the setting $\epsilon = 0.01$ significantly accelerates the rendering process without causing any noticeable quality degradation.

3.3 Learning

Since our rendering process is fully differentiable, NSVF can be optimized end-to-end through back-propagation by comparing the rendered outputs with a set of target images, without any 3D supervision. To this end, the following loss is minimized:

$$\mathcal{L} = \sum_{(\boldsymbol{p}_0, \boldsymbol{v}) \in R} \|\boldsymbol{C}(\boldsymbol{p}_0, \boldsymbol{v}) - \boldsymbol{C}^*(\boldsymbol{p}_0, \boldsymbol{v})\|_2^2 + \lambda \cdot \Omega\left(A(\boldsymbol{p}_0, \boldsymbol{v})\right), \tag{5}$$

where R is a batch of sampled rays, $\boldsymbol{C}^*$ is the ground-truth color of the camera ray, and $\Omega(.)$ is a beta-distribution regularizer proposed in Lombardi et al. (2019). Next, we propose a progressive training strategy to better facilitate learning and inference:

Voxel Initialization We start by learning implicit functions for an initial set of voxels subdividing an initial bounding box (with volume V) that roughly encloses the scene with sufficient margin. The initial voxel size is set to $l \approx \sqrt[3]{V/1000}$. If a coarse geometry (e.g. scanned point clouds or visual hull outputs) is available, the initial voxels can also be initialized by voxelizing the coarse geometry.

Self-Pruning Existing volume-based neural rendering works (Lombardi et al., 2019; Mildenhall et al., 2020) have shown that it is feasible to extract scene geometry on a coarse level after training. Based on this observation, we propose – *self-pruning* – a strategy to effectively remove non-essential voxels during training based on the coarse geometry information which can be further described using model's prediction on density. That is, we determine voxels to be pruned as follows:

$$V_i \text{ is pruned } \textbf{if} \min_{j=1...G} \exp(-\sigma(g_i(\boldsymbol{p}_j))) > \gamma, \ \boldsymbol{p}_j \in V_i, V_i \in \mathcal{V}, \tag{6}$$

where $\{\boldsymbol{p}_j\}_{j=1}^G$ are G uniformly sampled points inside the voxel V_i ($G = 16^3$ in our experiments), $\sigma(g_i(\boldsymbol{p}_j))$ is the predicted density at point $\boldsymbol{p}_j$, γ is a threshold ($\gamma = 0.5$ in all our experiments). Since this pruning process does not rely on other processing modules or input cues, we call it *self-pruning*. We perform self-pruning on voxels periodically after the coarse scene geometry emerges.

Progressive Training The above pruning strategy enables us to progressively adjust voxelization to the underlying scene structure and adaptively allocate computational and memory resources to important regions. Suppose that the learning starts with an initial ray-marching step size τ and voxel size l. After certain steps of training, we halve both τ and l for the next stage. Specifically, when halving the voxel size, we subdivide each voxel into 2^3 sub-voxels and the feature representations of the new vertices (i.e. $\tilde{g}(.)$ in § 3.1) are initialized via trilinear interpolation of feature representations at the original eight voxel vertices. Note that, when using embeddings as voxel representations, we essentially increase the model capacity progressively to learn more details of the scene. In our experiments, we train synthetic scenes with 4 stages and real scenes with 3 stages. An illustration of self-pruning and progressive training is shown in Figure 2.
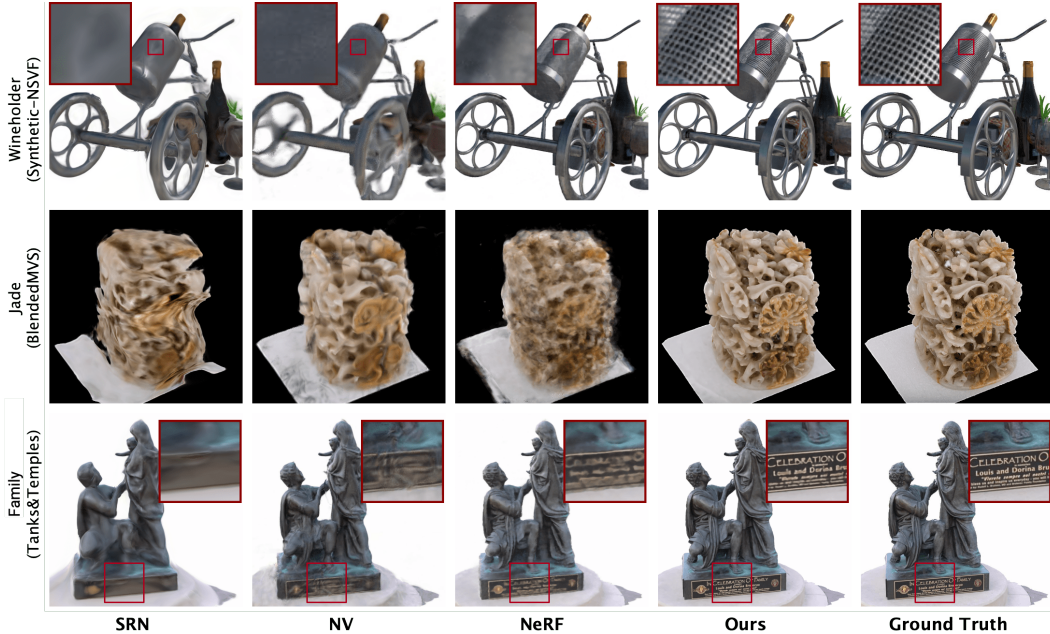
Figure 3: Comparisons on test views for scenes from the single-scene datasets. For *wineholder* and *family*, closeups are shown for clearer visual comparison.

4 Experiments

We evaluate the proposed NSVF on several tasks including multi-scene learning, rendering of dynamic and large-scale indoor scenes, and scene editing and composition. We also perform ablation studies to validate different kinds of feature representations and different options in progressive training. Please see the Appendix for more details on architecture, implementation, pre-processing of datasets and additional results. Please also refer to the supplemental video which shows the rendering quality.

4.1 Experimental Settings

Datasets (1) *Synthetic-NeRF:* The synthetic dataset used in Mildenhall et al. (2020) includes eight objects. (2) *Synthetic-NSVF:* We additionally render eight objects in the same resolution with more complex geometry and lighting effects. (3) *BlendedMVS:* We test on four objects from Yao et al. (2020). The rendered images are blended with the real images to have realistic ambient lighting.(4) *Tanks & Temples:* We evaluate on five objects from Knapitsch et al. (2017) where we use the images and label the object masks ourselves. (5) *ScanNet:* We use two real scenes from ScanNet (Dai et al., 2017). We extract both RGB and depth images from the original video.(6) *Maria Sequence:* This sequence is provided by Volucap with the meshes of 200 frames of a moving female. We render each mesh to create a dataset.

Baselines We adopt the following three recently proposed methods as baselines: Scene Representation Networks (SRN, Sitzmann et al., 2019b), Neural Volumes (NV, Lombardi et al., 2019), and Neural Radiance Fields (NeRF, Mildenhall et al., 2020), representing surface-based rendering, explicit and implicit volume rendering, respectively. See the Appendix for implementation details.

Implementation Details We model NSVF with a 32-dimentional learnable voxel embedding for each vertex, and apply positional encoding following (Mildenhall et al., 2020). The overall network architecture is shown in the Appendix Figure 9. For all scenes, we train NSVF using a batch size of 4 images on a single Nvidia V100 32G GPU, and for each image we sample 2048 rays. To improve training efficiency, we use a biased sampling strategy to only sample the rays which hits at least one voxel. For all the experiments, we prune the voxels periodically every 2500 steps and progressively halve the voxel and step sizes at 5k, 25k and 75k, separately. We have open-sourced our codebase at `https://github.com/facebookresearch/NSVF`

6

Table 1: The quantitative comparisons on test sets of four datasets. We use three metrics: PSNR ($\uparrow$), SSIM ($\uparrow$) and LPIPS ($\downarrow$) (Zhang et al., 2018) to evaluate the rendering quality. Scores are averaged over the testing images of all scenes, and we present the per-scene breakdown results in the Appendix. By default, NSVF is executed with early termination ($\epsilon = 0.01$). We also show results without using early termination ($\epsilon = 0$) denoted as NSVF^0.

| Models	Synthetic-NeRF			Synthetic-NSVF			BlendedMVS			Tanks and Temples		
	PSNR	SSIM	LPIPS	PSNR	SSIM	LPIPS	PSNR	SSIM	LPIPS	PSNR	SSIM	LPIPS
SRN	22.26	0.846	0.170	24.33	0.882	0.141	20.51	0.770	0.294	24.10	0.847	0.251
NV	26.05	0.893	0.160	25.83	0.892	0.124	23.03	0.793	0.243	23.70	0.834	0.260
NeRF	31.01	0.947	0.081	30.81	0.952	0.043	24.15	0.828	0.192	25.78	0.864	0.198
NSVF^0	**31.75**	**0.954**	0.048	**35.18**	**0.979**	**0.015**	26.89	**0.898**	0.114	**28.48**	**0.901**	0.155
NSVF	31.74	0.953	**0.047**	35.13	**0.979**	**0.015**	**26.90**	**0.898**	**0.113**	28.40	0.900	**0.153**
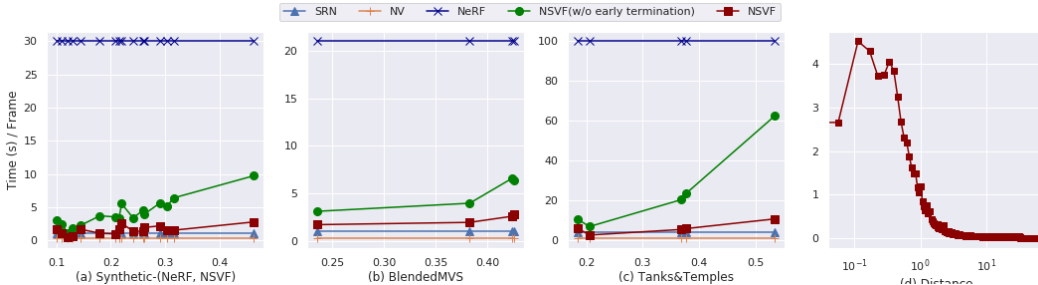
Figure 4: We report time taken to render one image for all the datasets in (a)-(c) where the x-axis stands for ascending foreground to background ratio and the y-axis for rendering time in second. We also show a plot curve for rendering time of NSVF on one synthetic scene in (d) when the camera is zooming out where the x-axis stands for the distance from the camera to the center of the object and the y-axis for rendering time in second.

4.2 Results

Quality Comparison We show the qualitative comparisons in Figure 3. SRN tends to produce overly smooth rendering and incorrect geometry; NV and NeRF work better but are still not able to synthesize images as sharply as NSVF does. NSVF can achieve photo-realistic results on various kinds of scenes with complex geometry, thin structures and lighting effects.

Also, as shown in Table 1, NSVF significantly outperforms the three baselines on all the four datasets across all metrics. Note that NSVF with early termination ($\epsilon = 0.01$) produces almost the same quality as NSVF without early termination (denoted as NSVF^0 in Table 1). This indicates that early termination would not cause noticeable quality degradation while significantly accelerating computation, as will be seen next.

Speed Comparison We provide speed comparisons on the models of four datasets in Figure 4 where we merge the results of *Synthetic-NeRF* and *Synthetic-NSVF* in the same figure considering their image sizes are the same. For our method, the average rendering time is correlated to the average ratio of foreground to background as shown in Figure 4 (a)-(c). That is because the higher the average ratio of foreground is, the more rays intersect with voxels. Thus, more evaluation time is needed. The average rendering time is also correlated to the number of intersected voxels. When a ray intersects a large number of voxels in the rendering of a solid object, early termination significantly reduces rendering time by avoiding many unnecessary accumulation steps behind the surface. These two factors can be seen in Figure 4 (d) where we show a zoom-out example.

For other methods, the rendering time is almost constant. This is because they have to evaluate all pixels with fixed steps, indicating a fixed number of points are sampled along each ray no matter whether the ray hits the scene or not, regardless of the scene complexity. In general, our method is around $10 \sim 20$ times faster than the state-of-the-art method NeRF, and gets close to SRN and NV.

Storage Comparison The storage usage for the network weights of NSVF varies from $3.2 \sim 16$MB (including around 2MB for MLPs), depending on the number of used voxels ($10 \sim 100$K). NeRF has two (coarse and fine) slightly deeper MLPs with a total storage usage of around 5MB.
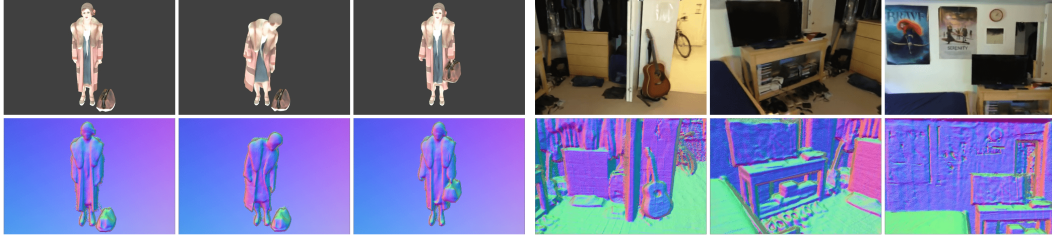
Figure 5: Our results on *Maria Sequence* (left) and *ScanNet* (right). We render testing trajectories and show three sampled frames in both RGB (top) and corresponding surface normals (below).

Models	PSNR↑	SSIM↑	LPIPS↓
NSVF	**32.04**	**0.965**	**0.020**
w/o POS	30.89	0.954	0.043
w/o EMB	27.02	0.931	0.077
w/o POS, EMB	24.47	0.906	0.118

NSVF w/o EMB   NSVF w/o POS   NSVF   Ground Truth

Figure 7: The table on the left shows quantitative comparison of NSVF w/o positional encoding (w/o POS), w/o voxel embeddings (w/o EMB) or w/o both (w/o POS,EMB). The figure on the right shows visual comparison against the ground truth image.

Figure 6: Scene composition and editing on the *Synthetic* datasets. The real images are presented bottom right.

Rendering of Indoor Scenes & Dynamic Scenes We demonstrate the effectiveness of our method on ScanNet dataset under challenging inside-out reconstruction scenarios. Our results are shown in Figure 5 where the initial voxels are built upon the point clouds from the depth images.

As shown in Figure 5, we also validate our approach on a corpus with dynamic scenes using the Maria Sequence. In order to accommodate temporal sequence with NSVF, we apply the hypernetwork proposed in Sitzmann et al. (2019b). We also include quantitative comparisons in the Appendix, which shows that NSVF outperforms all the baselines for both cases.

Multi-scene Learning We train a single model for all 8 objects from *Synthetic-NeRF* together with 2 additional objects (*wineholder*, *train*) from *Synthetic-NSVF*. We use different voxel embeddings for each scene while sharing the same MLPs to predict density and color. For comparison, we train NeRF model for the same datasets based on a hypernetwork (Ha et al., 2016). Without voxel embeddings, NeRF has to encode all the scene details with the network parameters, which leads to drastic quality degradation compared to single scene learning results. Table 2 shows that our method significantly outperforms NeRF on the multi-scene learning task.

Table 2: Results for multi-scene learning.

Models	PSNR↑	SSIM↑	LPIPS↓
NeRF	25.71	0.891	0.175
NSVF	**30.68**	**0.947**	**0.043**

Scene Editing and Scene Composition. As shown in Figure 6, the learnt multi-object model can be readily used to compose more complex scenes by duplicating and moving voxels, and be rendered in the same way without overhead. Furthermore, our approach also supports scene editing by directly adjusting the presence of sparse voxels (See the re-composition of *wineholder* in Figure 6).

Table 3: Ablation for progressive training.

R	PSNR↑	SSIM↑	LPIPS↓	Speed (s)
1	28.82	0.933	0.063	2.629
2	30.17	0.946	0.052	2.785
3	30.83	0.953	0.046	3.349
4	**30.89**	**0.954**	**0.043**	3.873

8

4.3 Ablation Studies

We use one object (*wineholder*) from the *Synthetic-NSVF* dataset which consists of parts with complex local patterns (grids) for ablation studies.

Effect of Voxel Representations Figure 7 shows the comparison on different kinds of feature representations for encoding a spatial location. Voxel embeddings bring larger improvements to the quality than using positional encoding. Also, with both positional encoding and voxel embeddings, the model achieves the best quality, especially for recovering high frequency patterns.

Effect of Progressive Training We also investigate different options for progressive training (see Table 3). Note that all the models are trained with voxel embeddings only. The performance is improved with more rounds of progressive training. But after a certain number of rounds, the quality improves only slowly while the rendering time increases. Based on this observation, our model performs 3-4 rounds of progressive training in the experiments.

5 Related Work

Neural Rendering Recent works have shown impressive results by replacing or augmenting the traditional graphics rendering with neural networks, which is typically referred to as *neural rendering*. We refer the reader to recent surveys for neural rendering (Tewari et al., 2020; Kato et al., 2020).

- **Novel View Synthesis with 3D inputs:** DeepBlending (Hedman et al., 2018) predicts blending weights for the image-based rendering on a geometric proxy. Other methods (Thies et al., 2019; Kim et al., 2018; Liu et al., 2019a, 2020; Meshry et al., 2019; Martin Brualla et al., 2018; Aliev et al., 2019) first render a given geometry with explicit or neural textures into coarse RGB images or feature maps which are then translated into high-quality images. However, these works need 3D geometry as input and the performance would be affected by the quality of the geometry.

- **Novel View Synthesis without 3D inputs:** Other approaches learn scene representations for novel-view synthesis from 2D images. Generative Query Networks (GQN) (Eslami et al., 2018) learn a vectorized embedding of a 3D scene and render it from novel views. However, they do not learn geometric scene structure as explicitly as NSVF, and their renderings are rather coarse. Following-up works learned more 3D-structure aware representations and accompanying renderers (Flynn et al., 2016; Zhou et al., 2018; Mildenhall et al., 2019) with Multiplane Images (MPIs) as proxies, which only render a restricted range of novel views interpolating input views. Nguyen-Phuoc et al. (2018, 2019); Liu et al. (2019c) use a CNN-based decoder for differentiable rendering to render a scene represented as coarse-grained voxel grids. However, this CNN-based decorder cannot ensure view consistency due to 2D convolution kernels.

Neural Implicit Representations. Implicit representations have been studied to model 3D geometry with neural networks. Compared to explicit representations (such as point cloud, mesh, voxels), implicit representations are continuous and have high spatial resolution. Most works require 3D supervision during training to infer the SDF value or the occupancy probability of any 3D point (Michalkiewicz et al., 2019; Mescheder et al., 2019; Chen and Zhang, 2019; Park et al., 2019; Peng et al., 2020), while other works learn 3D representations only from images with differentiable renderers (Liu et al., 2019d; Saito et al., 2019, 2020; Niemeyer et al., 2019; Jiang et al., 2020).

6 Conclusion

We propose NSVF, a hybrid neural scene representations for fast and high-quality free-viewpoint rendering. Extensive experiments show that NSVF is typically over 10 times faster than the state-of-the-art (namely, NeRF) while achieving better quality. NSVF can be easily applied to scene editing and composition. We also demonstrate a variety of challenging tasks, including multi-scene learning, free-viewpoint rendering of a moving human, and large-scale scene rendering.

7 Broader Impact

NSVF provides a new way to learn a neural implicit scene representation from images that is able to better allocate network capacity to relevant parts of a scene. In this way, it enables learning representations of large-scale scenes at higher detail than previous approaches, which also leads to higher visual quality of the rendered images. In addition, the proposed representation enables much faster rendering than the state-of-the-art, and enables more convenient scene editing and compositing. This new approach to 3D scene modeling and rendering from images complements and partially improves over established computer graphics concepts, and opens up new possibilities in many applications, such as mixed reality, visual effects, and training data generation for computer vision tasks. At the same time it shows new ways to learn spatially-aware scene representations of potential relevance in other domains, such as object scene understanding, object recognition, robot navigation, or training data generation for image-based reconstruction.

The ability to capture and re-render, only from 2D images, models of real world scenes at very high visual fidelity, also enables the possibility to reconstruct and re-render humans in a scene. Appropriate privacy preserving steps should be considered if applying this method to images comprising identifiable individuals.

References

Kara-Ali Aliev, Dmitry Ulyanov, and Victor Lempitsky. 2019. Neural point-based graphics. *arXiv preprint arXiv:1906.08240*.

Z. Chen and H. Zhang. 2019. Learning implicit fields for generative shape modeling. In *2019 IEEE/CVF Conference on Computer Vision and Pattern Recognition (CVPR)*, pages 5932–5941.

Angela Dai, Angel X. Chang, Manolis Savva, Maciej Halber, Thomas Funkhouser, and Matthias Nießner. 2017. Scannet: Richly-annotated 3d reconstructions of indoor scenes. In *Proc. Computer Vision and Pattern Recognition (CVPR), IEEE*.

SM Ali Eslami, Danilo Jimenez Rezende, Frederic Besse, Fabio Viola, Ari S Morcos, Marta Garnelo, Avraham Ruderman, Andrei A Rusu, Ivo Danihelka, Karol Gregor, et al. 2018. Neural scene representation and rendering. *Science*, 360(6394):1204–1210.

John Flynn, Michael Broxton, Paul Debevec, Matthew DuVall, Graham Fyffe, Ryan Overbeck, Noah Snavely, and Richard Tucker. 2019. Deepview: View synthesis with learned gradient descent. *International Conference on Computer Vision and Pattern Recognition (CVPR)*.

John Flynn, Ivan Neulander, James Philbin, and Noah Snavely. 2016. Deepstereo: Learning to predict new views from the world's imagery. In *Computer Vision and Pattern Recognition (CVPR)*.

David Ha, Andrew Dai, and Quoc Le. 2016. Hypernetworks.

Eric Haines. 1989. *Essential Ray Tracing Algorithms*, page 33–77. Academic Press Ltd., GBR.

Peter Hedman, Julien Philip, True Price, Jan-Michael Frahm, George Drettakis, and Gabriel Brostow. 2018. Deep blending for free-viewpoint image-based rendering. *ACM Trans. Graph.*, 37(6):257:1–257:15.

Yue Jiang, Dantong Ji, Zhizhong Han, and Matthias Zwicker. 2020. Sdfdiff: Differentiable rendering of signed distance fields for 3d shape optimization. In *The IEEE/CVF Conference on Computer Vision and Pattern Recognition (CVPR)*.

Hiroharu Kato, Deniz Beker, Mihai Morariu, Takahiro Ando, Toru Matsuoka, Wadim Kehl, and Adrien Gaidon. 2020. Differentiable rendering: A survey. *arXiv preprint arXiv:2006.12057*.

Hyeongwoo Kim, Pablo Garrido, Ayush Tewari, Weipeng Xu, Justus Thies, Matthias Nießner, Patrick Pérez, Christian Richardt, Michael Zollöfer, and Christian Theobalt. 2018. Deep video portraits. *ACM Transactions on Graphics (TOG)*, 37.

Arno Knapitsch, Jaesik Park, Qian-Yi Zhou, and Vladlen Koltun. 2017. Tanks and temples: Benchmarking large-scale scene reconstruction. *ACM Transactions on Graphics*, 36(4).

Samuli Laine and Tero Karras. 2010. Efficient sparse voxel octrees–analysis, extensions, and implementation.

Lingjie Liu, Weipeng Xu, Marc Habermann, Michael Zollhöfer, Florian Bernard, Hyeongwoo Kim, Wenping Wang, and Christian Theobalt. 2020. Neural human video rendering by learning dynamic textures and rendering-to-video translation. *IEEE Transactions on Visualization and Computer Graphics*, PP:1–1.

Lingjie Liu, Weipeng Xu, Michael Zollhoefer, Hyeongwoo Kim, Florian Bernard, Marc Habermann, Wenping Wang, and Christian Theobalt. 2019a. Neural rendering and reenactment of human actor videos. *ACM Transactions on Graphics (TOG)*.

Shaohui Liu, Yinda Zhang, Songyou Peng, Boxin Shi, Marc Pollefeys, and Zhaopeng Cui. 2019b. Dist: Rendering deep implicit signed distance function with differentiable sphere tracing. *arXiv preprint arXiv:1911.13225*.

Shichen Liu, Weikai Chen, Tianye Li, and Hao Li. 2019c. Soft rasterizer: Differentiable rendering for unsupervised single-view mesh reconstruction. *arXiv preprint arXiv:1901.05567*.

Shichen Liu, Shunsuke Saito, Weikai Chen, and Hao Li. 2019d. Learning to infer implicit surfaces without 3d supervision. In *Advances in Neural Information Processing Systems*, pages 8295–8306.

Stephen Lombardi, Tomas Simon, Jason Saragih, Gabriel Schwartz, Andreas Lehrmann, and Yaser Sheikh. 2019. Neural volumes: Learning dynamic renderable volumes from images. *ACM Transactions on Graphics (TOG)*, 38(4):65.

Ricardo Martin Brualla, Peter Lincoln, Adarsh Kowdle, Christoph Rhemann, Dan Goldman, Cem Keskin, Steve Seitz, Shahram Izadi, Sean Fanello, Rohit Pandey, Shuoran Yang, Pavel Pidlypenskyi, Jonathan Taylor, Julien Valentin, Sameh Khamis, Philip Davidson, and Anastasia Tkach. 2018. Lookingood: Enhancing performance capture with real-time neural re-rendering. volume 37.

Lars Mescheder, Michael Oechsle, Michael Niemeyer, Sebastian Nowozin, and Andreas Geiger. 2019. Occupancy networks: Learning 3d reconstruction in function space. In *Proceedings IEEE Conf. on Computer Vision and Pattern Recognition (CVPR)*.

Moustafa Meshry, Dan B. Goldman, Sameh Khamis, Hugues Hoppe, Rohit Pandey, Noah Snavely, and Ricardo Martin-Brualla. 2019. Neural rerendering in the wild. In *Computer Vision and Pattern Recognition (CVPR)*.

Mateusz Michalkiewicz, Jhony K. Pontes, Dominic Jack, Mahsa Baktashmotlagh, and Anders Eriksson. 2019. Implicit surface representations as layers in neural networks. In *The IEEE International Conference on Computer Vision (ICCV)*.

Ben Mildenhall, Pratul P Srinivasan, Rodrigo Ortiz-Cayon, Nima Khademi Kalantari, Ravi Ramamoorthi, Ren Ng, and Abhishek Kar. 2019. Local light field fusion: Practical view synthesis with prescriptive sampling guidelines. *ACM Transactions on Graphics (TOG)*, 38(4):1–14.

Ben Mildenhall, Pratul P Srinivasan, Matthew Tancik, Jonathan T Barron, Ravi Ramamoorthi, and Ren Ng. 2020. Nerf: Representing scenes as neural radiance fields for view synthesis. *arXiv preprint arXiv:2003.08934*.

Thu Nguyen-Phuoc, Chuan Li, Lucas Theis, Christian Richardt, and Yong-Liang Yang. 2019. Hologan: Unsupervised learning of 3d representations from natural images. In *Proceedings of the IEEE International Conference on Computer Vision*, pages 7588–7597.

Thu H Nguyen-Phuoc, Chuan Li, Stephen Balaban, and Yongliang Yang. 2018. Rendernet: A deep convolutional network for differentiable rendering from 3d shapes. In *Advances in Neural Information Processing Systems (NIPS)*.

Michael Niemeyer, Lars Mescheder, Michael Oechsle, and Andreas Geiger. 2019. Differentiable volumetric rendering: Learning implicit 3d representations without 3d supervision. *arXiv preprint arXiv:1912.07372*.

Jeong Joon Park, Peter Florence, Julian Straub, Richard Newcombe, and Steven Lovegrove. 2019. Deepsdf: Learning continuous signed distance functions for shape representation. *International Conference on Computer Vision and Pattern Recognition (CVPR)*.

Songyou Peng, Michael Niemeyer, Lars M. Mescheder, Marc Pollefeys, and Andreas Geiger. 2020. Convolutional occupancy networks. *ArXiv*, abs/2003.04618.

Steven M Rubin and Turner Whitted. 1980. A 3-dimensional representation for fast rendering of complex scenes. In *Proceedings of the 7th annual conference on Computer graphics and interactive techniques*, pages 110–116.

Shunsuke Saito, Zeng Huang, Ryota Natsume, Shigeo Morishima, Angjoo Kanazawa, and Hao Li. 2019. Pifu: Pixel-aligned implicit function for high-resolution clothed human digitization. *2019 IEEE/CVF International Conference on Computer Vision (ICCV)*, pages 2304–2314.

Shunsuke Saito, Tomas Simon, Jason Saragih, and Hanbyul Joo. 2020. Pifuhd: Multi-level pixel-aligned implicit function for high-resolution 3d human digitization. In *Proceedings of the IEEE Conference on Computer Vision and Pattern Recognition*.

Harry Shum and Sing Bing Kang. 2000. Review of image-based rendering techniques. In *Visual Communications and Image Processing 2000*, volume 4067, pages 2 – 13. International Society for Optics and Photonics, SPIE.

Vincent Sitzmann, Justus Thies, Felix Heide, Matthias Niessner, Gordon Wetzstein, and Michael Zollhofer. 2019a. Deepvoxels: Learning persistent 3d feature embeddings. In *Computer Vision and Pattern Recognition (CVPR)*.

Vincent Sitzmann, Michael Zollhöfer, and Gordon Wetzstein. 2019b. Scene representation networks: Continuous 3d-structure-aware neural scene representations. In *Advances in Neural Information Processing Systems*, pages 1119–1130.

Richard Szeliski. 2010. *Computer vision: algorithms and applications*. Springer Science & Business Media.

A. Tewari, O. Fried, J. Thies, V. Sitzmann, S. Lombardi, K. Sunkavalli, R. Martin-Brualla, T. Simon, J. Saragih, M. Nießner, R. Pandey, S. Fanello, G. Wetzstein, J.-Y. Zhu, C. Theobalt, M. Agrawala, E. Shechtman, D. B Goldman, and M. Zollhöfer. 2020. State of the Art on Neural Rendering. *Computer Graphics Forum (EG STAR 2020)*.

Justus Thies, Michael Zollhöfer, and Matthias Nießner. 2019. Deferred neural rendering: image synthesis using neural textures. *ACM Transactions on Graphics*, 38.

Ashish Vaswani, Noam Shazeer, Niki Parmar, Jakob Uszkoreit, Llion Jones, Aidan N Gomez, Łukasz Kaiser, and Illia Polosukhin. 2017. Attention is all you need. In *Advances in neural information processing systems*, pages 5998–6008.

Xinchen Yan, Jimei Yang, Ersin Yumer, Yijie Guo, and Honglak Lee. 2016. Perspective transformer nets: Learning single-view 3d object reconstruction without 3d supervision. In *Advances in neural information processing systems*, pages 1696–1704.

Yao Yao, Zixin Luo, Shiwei Li, Jingyang Zhang, Yufan Ren, Lei Zhou, Tian Fang, and Long Quan. 2020. Blendedmvs: A large-scale dataset for generalized multi-view stereo networks. *Computer Vision and Pattern Recognition (CVPR)*.

Cha Zhang and Tsuhan Chen. 2004. A survey on image-based rendering—representation, sampling and compression. *Signal Processing: Image Communication*, 19(1):1–28.

Richard Zhang, Phillip Isola, Alexei A Efros, Eli Shechtman, and Oliver Wang. 2018. The unreasonable effectiveness of deep features as a perceptual metric. In *CVPR*.

Tinghui Zhou, Richard Tucker, John Flynn, Graham Fyffe, and Noah Snavely. 2018. Stereo magnification: Learning view synthesis using multiplane images. In *SIGGRAPH*.

A Additional Details of the Method

A.1 Algorithm

We present the algorithm of rendering with NSVF as follows in Algorithm 1. We additionally return the transparency A, and the expected depth Z which can be further used for visualizing the normal with finite difference.

Algorithm 1: Neural Rendering with NSVF

Input: camera $\boldsymbol{p}_0$, ray direction $\boldsymbol{v}$, step size τ, threshold ϵ, voxels $\mathcal{V} = \{V_1, \ldots, V_K\}$, background $\boldsymbol{c}_{\mathrm{bg}}$, background maximum depth $z_{\max}$, parameters of the MLPs θ

Initialize: transparency $A = 1$, color $\boldsymbol{C} = \boldsymbol{0}$, expected depth $Z = 0$

Ray-voxel Intersection: Return all the intersections of the ray with k intersected voxels, sorted from near to far: $z_{t_1}^{\mathrm{in}}, z_{t_1}^{\mathrm{out}}, \ldots, z_{t_k}^{\mathrm{in}}, z_{t_k}^{\mathrm{out}}$, where $\{t_1, \ldots, t_k\} \subset \{1 \ldots K\}, k < K$;

if $k > 0$ **then**

    Stratified sampling: $z_1, \ldots, z_m$ with step size τ, where $z_1 \geq z_{t_1}^{\mathrm{in}}$ and $z_m \leq z_{t_k}^{\mathrm{out}}$;

    Include voxel boundaries: $\tilde{z}_1, \ldots \tilde{z}_{2k+m} \leftarrow \mathrm{sort}\left(z_1, \ldots, z_m; z_{t_1}^{\mathrm{in}}, z_{t_1}^{\mathrm{out}}, \ldots, z_{t_k}^{\mathrm{in}}, z_{t_k}^{\mathrm{out}}\right)$;

    for $j \leftarrow 1$ **to** $2k + m - 1$ **do**

        Obtain midpoints and intervals: $\hat{z}_j \leftarrow \frac{\tilde{z}_j + \tilde{z}_{j+1}}{2}, \Delta_j \leftarrow \tilde{z}_{j+1} - \tilde{z}_j$;

        if $A > \epsilon$ **and** $\Delta_j > 0$ **and** $\boldsymbol{p}(\hat{z}_j) \in V_i (\exists i \in \{t_1, \ldots, t_k\})$ **then**

            $\alpha \leftarrow \exp\left(-\sigma_\theta\left(g_i(\boldsymbol{p}(\hat{z}_j))\right) \cdot \Delta_j\right), \quad \boldsymbol{c} \leftarrow \boldsymbol{c}_\theta\left(g_i(\boldsymbol{p}(\hat{z}_j)), \boldsymbol{v}\right)$;

            $\boldsymbol{C} \leftarrow \boldsymbol{C} + A \cdot (1 - \alpha) \cdot \boldsymbol{c}, \quad Z \leftarrow Z + A \cdot (1 - \alpha) \cdot \hat{z}_j, \quad A \leftarrow A \cdot \alpha$;

$\boldsymbol{C} \leftarrow \boldsymbol{C} + A \cdot \boldsymbol{c}_{\mathrm{bg}}, \quad Z \leftarrow Z + A \cdot z_{\max}$;

Return: $\boldsymbol{C}, Z, A$

A.2 Overall Pipeline

We present the illustrations of the overall pipeline to better demonstrate the proposed approach in Figure 8. For any given camera position $\boldsymbol{p}_0$ and the ray direction $\boldsymbol{v}$, we render its color $\boldsymbol{c}$ with NSVF by first intersecting the ray with a set of sparse voxels, and sampling and accumulating the color and density inside every intersected voxel, which are predicted by neural networks.
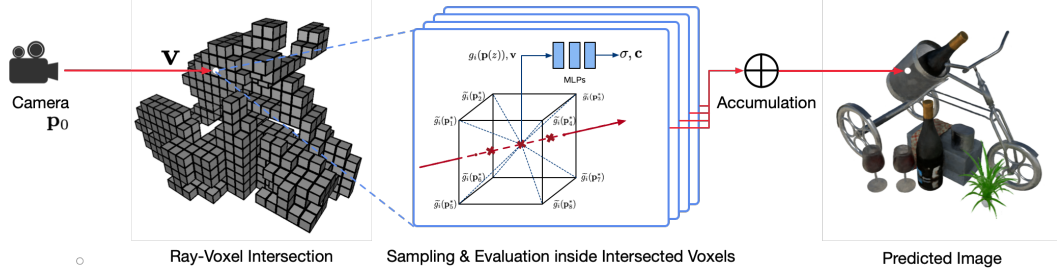
Figure 8: Illustration of the differenitable volume rendering procedure with NSVF. For any given camera position $\boldsymbol{p}_0$ and the ray direction $\boldsymbol{v}$, we first intersect the ray with a set of sparse voxels, then predict the colors and densities with neural networks for points sampled along the ray inside voxels, and accumulate the colors and densities of the sampled points to get the rendered color $\boldsymbol{C}(\boldsymbol{p}_0, \boldsymbol{v})$.

B Additional Experimental Settings

B.1 Datasets

We present more details about the datasets we used. We conduct the experiments of single-scene learning on five datasets, including three synthetic datasets and two real datasets:

- *Synthetic-NeRF.* We use the NeRF (Mildenhall et al., 2020) synthetic dataset which includes eight objects rendered with path tracing. Each object is rendered to produce 100 views for training and 200 for testing at 800×800 pixels.

- *Synthetic-NSVF.* To demonstrate the ability of NSVF to handle various conditions, we additionally render eight objects in 800×800 with more complex geometry and lighting effects. Details on the original source files and license information are given below:

  - Wineholder(CC-0) `https://www.blendswap.com/blend/15899`
  - Steamtrain(CC-BY-NC) `https://www.blendswap.com/blend/16763`
  - Toad(CC-0) `https://www.blendswap.com/blend/13078`
  - Robot(CC-BY-SA) `https://www.blendswap.com/blend/10597`
  - Bike(CC-BY) `https://www.blendswap.com/blend/8850`
  - Palace(CC-BY-NC-SA) `https://www.blendswap.com/blend/14878`
  - Spaceship(CC-BY) `https://www.blendswap.com/blend/5349`
  - Lifestyle(CC-BY) `https://www.blendswap.com/blend/8909`

- *BlendedMVS.* We test on four objects of a recent synthetic MVS dataset, BlendedMVS (Yao et al., 2020) [2]. The rendered images are blended with the real images to have realistic ambient lighting. The image resolution is 768×576. One eighth of the images are held out as test sets.

- *Tanks & Temples.* We evaluate on five objects of Tanks and Temples (Knapitsch et al., 2017) [3] real scene dataset. We label the object masks ourselves with the software of Altizure [4], and sample One eighth of the images for testing. The image resolution is 1920×1080.

- *ScanNet.* We use two real scenes of an RGB-D video dataset for large-scale indoor scenes, ScanNet (Dai et al., 2017)[5]. We extract both the RGB and depth images of which we randomly sample 20% as training set and use the rest for testing. The image is scaled to 640×480.

For the multi-scene learning, we show our result of training with all the scenes of *Synthetic-NeRF* and two out of *Synthetic-NSVF*, and the result of training with all the frames of a moving human:

- *Maria Sequence.* This sequence is provided by *Volucap* with the meshes of 200 frames of a moving female. We render each mesh from 50 viewpoints sampled on the upper hemisphere at 1024×1024 pixels. We also render 50 additional views in a circular trajectory as the test set.

B.2 Implementation Details

Architecture The proposed model assigns a 32-dimentional learnable voxel embedding to each vertex, and applies positional encoding with maximum frequency as $L = 6$ (Mildenhall et al., 2020) to the feature embedding aggregated by eight voxel embeddings of the corresponding voxel via trilinear interpolation. As a comparison, we also train our model without positional encoding where we set the voxel embedding dimension $d = 416$ in order to have comparable feature vectors as the complete model. We use around 1000 initial voxels for each scene. The final number of voxels after pruning and progressive training varies from 10k to 100k (the exact number of voxels differs scene by scene due to varying sizes and shapes), with an effective number of $0.32 \sim 3.2\text{M}$ learnable parameters in our default voxel embedding settings.

The overall network architecture of our default model is illustrated in Figure 9 with $\sim 0.5\text{M}$ parameters, not including voxel embeddings. Note that, our implementation of the MLP is slightly shallower than many of the existing works (Sitzmann et al., 2019b; Niemeyer et al., 2019; Mildenhall et al., 2020). By utilizing the voxel embeddings to store local information in a distributed way, we argue that it is sufficient to learn a small MLP to gather voxel information and make accurate predictions.
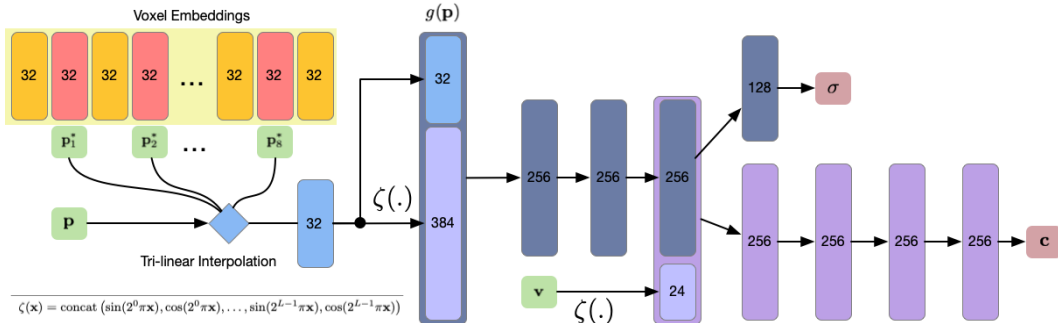
---

[2] `https://github.com/YoYo000/BlendedMVS`
[3] `https://tanksandtemples.org/download/`
[4] `https://github.com/altizure/altizure-sdk-offline`
[5] `http://www.scan-net.org/`

$$\zeta(\mathbf{x}) = \text{concat}\left(\sin(2^0 \pi \mathbf{x}), \cos(2^0 \pi \mathbf{x}), \ldots, \sin(2^{L-1} \pi \mathbf{x}), \cos(2^{L-1} \pi \mathbf{x})\right)$$

Figure 9: A visualization of the proposed NSVF architecture. For any input $(\boldsymbol{p}, \boldsymbol{v})$, the model first obtains the feature representation by querying and interpolating the voxel embeddings with the 8 corresponding voxel vertices, and then uses the computed feature to further predicts $(\sigma, \boldsymbol{c})$ using a MLP shared by all voxels.

Training & Inference   We train NSVF using a batch size of 4 images on a single Nvidia V100 32G GPU, and for each image we sample 2048 rays. To improve training efficiency, we use a biased sampling strategy to sample rays where it hits at least one voxel. We use Adam optimizer with an initial learning rate of 0.001 and linear decay scheduling. By default, we set the step size $\tau = l/8$, while the initial voxel size (l) is determined as discussed in § 3.3.

For all experiments, we prune the voxels with Eq (6) periodically for every 2500 steps. All our models are trained with $100 \sim 150$k iterations by progressively halving the voxel and step sizes at 5k, 25k and 75k, separately. At inference time, we use the threshold of $\epsilon = 0.01$ for early termination for all models. As a comparison, we also conduct experiments without setting up early termination. Our model is implemented in PyTorch using Fairseq framework[6].

Evaluation   We measure the quality on test sets with three metrics: PSNR, SSIM and LPIPS (Zhang et al., 2018). For the comparisons in speed, we render NSVF and the baselines with one image per batch and calculate the average rendering time using a single Nvidia V100 GPU.

Multi-scene Learning   Our experiments also require learning NSVF on multiple objects where a voxel location may be shared by different objects. In this work, we present two ways to tackle this issue. First, we use the navie approach that learns saperate embedding matrices for each object and only the MLP are shared. This is well suitable when the categories of target objects are quite distinct, and this can essentially increase the model capacity by extending the number of embeddings infinitely. We validate this method for the multi-scene learning task on all 8 scenes from *Synthetic-NeRF* together with 2 additional scenes (*wineholder, train*) from *Synthetic-NSVF*.

However, when modeling multiple objects that have similarities (e.g., a class of objects, or a moving sequence of the target object), it is more suitable to have shared voxel representations. Here we learn a set of voxel embeddings for each voxel position, while maintaining a unique embedding vector for each object. We compute the final voxel representation based on hypernetworks (Sitzmann et al., 2019b) with the object embedding as the input. We show our results on *Maria Sequence*.

B.3   Additional Baseline Details

Scene Representation Networks (SRN, Sitzmann et al., 2019b)   We use the original code open-sourced by the authors [7]. To enable training on higher resolution images, we employ the ray-based sampling strategy that is similarly used in neural volumes and NeRF. We use the batch size of 8 and 5120 rays per image. We found that clipping gradient norm to 1 greatly improves stability during training. All models are trained for 300k iterations.

---

[6] https://github.com/pytorch/fairseq
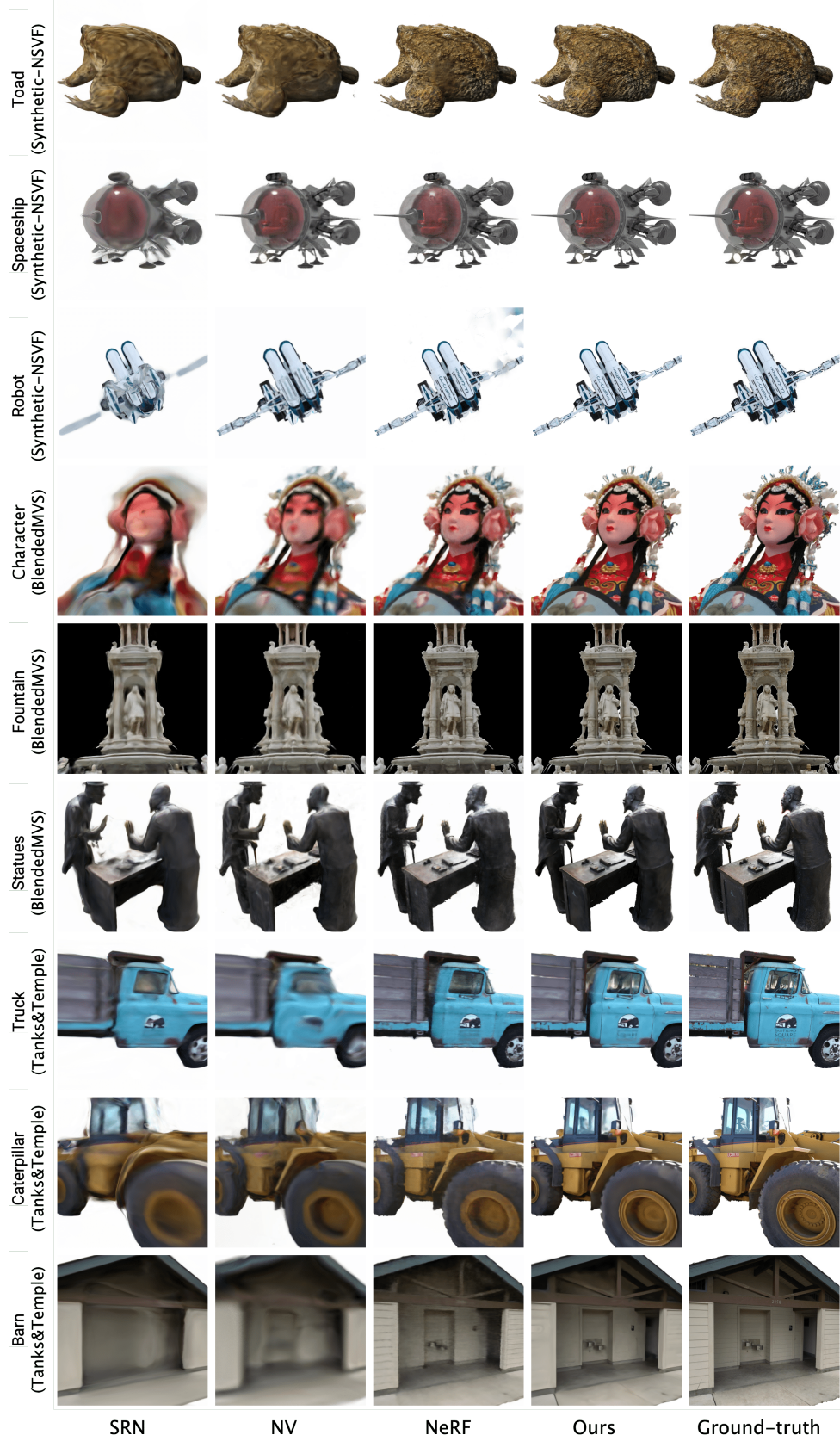[7] https://github.com/vsitzmann/scene-representation-networks

Figure 10: Additional examples and comparisons sampled from *Synthetic-NSVF*, *BlendedMVS* and *Tanks&Temples* datasets. Please see more results in the supplemental video.

Figure 11: An example of zooming in and out without any visible artifacts
.

Neural Volumes (NV, Lombardi et al., 2019)   We use the original code opensourced by the authors [8]. We use batch size of 8 and 128×128 rays per image. The center and scale of each scene are determined using the visual hull to place the scene within a cube that spans from -1 to 1 on each axis, as required by implementation. All models are trained for 40k iterations.

Neural Radiance Fields (NeRF, Mildenhall et al., 2020)   We use the NeRF code opensourced by the authors [9] and train on a single scene with the default settings used in NeRF with 100k-150k iterations. We scale the bounding box of each scene used in NSVF so that the bounding box lies within a cube of side length 2 centered at origin. To train on multiple scenes, we employ the auto-decoding scheme using a hypernetwork as described in SRN (Sitzmann et al., 2019b). We use a 1-layer hypernetwork to predict weights for all the scenes. The latent code dimension is 256.

C   Additional Results

C.1   Per-scene breakdown

We show the per-scene breakdown analysis of the quantitative results presented in the main paper (Table 1) for the four datasets (*Synthetic-NeRF*, *Synthetic-NSVF*, *BlendedMVS* and *Tanks&Temples*). Table 4 reports the comparisons with the three baselines in three metrics. Our approach achieves the best performance on both PSNR and LPIPS metrics across almost all the scenes, especially for datasets with real objects.

C.2   Additional Examples

In Figure 10, we present additional examples for individual scenes not shown in the main paper. We would like to highlight how well our method performs across a wide variety of scenes, showing much better visual fidelity than all the baselines.

C.3   Additional Analysis

Effects of Voxel Sizes.   In Table 5, we show additional comparison on *wineholder* where we fix the ray marching step size as the initial values, while training the model with different voxel sizes. The first column shows the ratio compared to the initial voxel size. It is clear that reducing the voxel size helps improve the rendering quality, indicating that progressively increasing the model's capacity alone helps model details better for free-viewpoint rendering.

Geometry Reconstruction Accuracy   We would like to expand on the observation that we have briefly touched on in the main paper regarding the nature of surface-based and volume-based renderers.

---

[8]https://github.com/facebookresearch/neuralvolumes
[9]https://github.com/bmild/nerf

18

Table 4: Detailed breakdown of quantitative metrics of individual scenes for all 4 datasets for our method and 3 baselines. All scores are averaged over the testing images.

	Chair	Drums	Lego	Mic	Materials	Ship	Hotdog	Ficus
Synthetic-NeRF								
PSNR↑								
SRN	26.96	17.18	20.85	26.85	18.09	20.60	26.81	20.73
NV	28.33	22.58	26.08	27.78	24.22	23.93	30.71	24.79
NeRF	33.00	25.01	**32.54**	32.91	29.62	28.65	36.18	30.13
Ours	**33.19**	**25.18**	32.29	**34.27**	**32.68**	27.93	**37.14**	**31.23**
SSIM↑								
SRN	0.910	0.766	0.809	0.947	0.808	0.757	0.923	0.849
NV	0.916	0.873	0.880	0.946	0.888	0.784	0.944	0.910
NeRF	0.967	0.925	**0.961**	0.980	0.949	**0.856**	0.974	0.964
Ours	**0.968**	**0.931**	0.960	**0.987**	**0.973**	0.854	**0.980**	**0.973**
LPIPS↓								
SRN	0.106	0.267	0.200	0.063	0.174	0.299	0.100	0.149
NV	0.109	0.214	0.175	0.107	0.130	0.276	0.109	0.162
NeRF	0.046	0.091	0.050	0.028	0.063	0.206	0.121	0.044
Ours	**0.043**	**0.069**	**0.029**	**0.010**	**0.021**	**0.162**	**0.025**	**0.017**

	Wineholder	Steamtrain	Toad	Robot	Bike	Palace	Spaceship	Lifestyle
Synthetic-NSVF								
PSNR↑								
SRN	20.74	25.49	25.36	22.27	23.76	24.45	27.99	24.58
NV	21.32	25.31	24.63	24.74	26.65	26.38	29.90	27.68
NeRF	28.23	30.84	29.42	28.69	31.77	31.76	34.66	31.08
Ours	**32.04**	**35.13**	**33.25**	**35.24**	**37.75**	**34.05**	**39.00**	**34.60**
SSIM↑								
SRN	0.850	0.923	0.822	0.904	0.926	0.792	0.945	0.892
NV	0.828	0.900	0.813	0.927	0.943	0.826	0.956	0.941
NeRF	0.920	0.966	0.920	0.960	0.970	0.950	0.980	0.946
Ours	**0.965**	**0.986**	**0.968**	**0.988**	**0.991**	**0.969**	**0.991**	**0.971**
LPIPS↓								
SRN	0.224	0.082	0.204	0.120	0.075	0.240	0.061	0.120
NV	0.204	0.121	0.192	0.096	0.067	0.173	0.056	0.088
NeRF	0.096	0.031	0.069	0.038	0.019	0.031	0.016	0.047
Ours	**0.020**	**0.010**	**0.032**	**0.007**	**0.004**	**0.018**	**0.006**	**0.020**

	Jade	Fountain	Char	Statues	Ignatius	Truck	Barn	Cate	Family
BlendedMVS					**Tanks& Temple**				
PSNR↑									
SRN	18.57	21.04	21.98	20.46	26.70	22.62	22.44	21.14	27.57
NV	22.08	22.71	24.10	23.22	26.54	21.71	20.82	20.71	28.72
NeRF	21.65	25.59	25.87	23.48	25.43	25.36	24.05	23.75	30.29
Ours	**26.96**	**27.73**	**27.95**	**24.97**	**27.91**	**26.92**	**27.16**	**26.44**	**33.58**
SSIM↑									
SRN	0.715	0.717	0.853	0.794	0.920	0.832	0.741	0.834	0.908
NV	0.750	0.762	0.876	0.785	0.922	0.793	0.721	0.819	0.916
NeRF	0.750	0.860	0.900	0.800	0.920	0.860	0.750	0.860	0.932
Ours	**0.901**	**0.913**	**0.921**	**0.858**	**0.930**	**0.895**	**0.823**	**0.900**	**0.954**
LPIPS↓									
SRN	0.323	0.291	0.208	0.354	0.128	0.266	0.448	0.278	0.134
NV	0.292	0.263	0.140	0.277	0.117	0.312	0.479	0.280	0.111
NeRF	0.264	0.149	0.149	0.206	0.111	0.192	0.395	0.196	0.098
Ours	**0.094**	**0.113**	**0.074**	**0.171**	**0.106**	**0.148**	**0.307**	**0.141**	**0.063**

Table 5: Effect of voxel size on the *wineholder* test set.

Voxel	PSNR↑	SSIM↑	LPIPS↓	Speed (s/frame)
1	28.82	0.933	0.063	2.629
1/2	29.22	0.938	0.057	1.578
1/4	29.70	0.944	0.052	**1.369**
1/8	**30.17**	**0.948**	**0.047**	1.515

As we have mentioned, surface-based rendering methods (e.g. SRN) require an accurate surface to be able to learn the color well. A failure case where geometry fails to be learnt is seen in the "Character" scene in Figure 10. In addition, we observe that SRN frequently gets stuck in a local minima so that the geometry is incorrect but is nevertheless approximately multi-view consistent. We find that this phenomenon occurs much less frequently in volume rendering methods including ours. NV, due to limited spatial resolution, is unable to capture high frequency details. NeRF generally works well while is still not able to synthesize images as sharply as NSVF does. Furthermore, NeRF suffers from a slow rendering process due to its inefficient sampling strategy. For instance. it takes 30s to render an 800×800 image with NeRF.

Zoom-In & -Out Our model naturally supports zooming in and out for a trained object. We show the results in Figure 11.

Table 6: Quantitative results on *Wineholder* of NSVF with different threshold ϵ for early termination.

ϵ	PSNR↑	SSIM↑	LPIPS↓	Speed (s/frame)
0.000	31.93	0.965	0.021	4.0
0.001	32.03	0.965	0.020	2.1
0.010	**32.04**	**0.965**	**0.020**	2.0
0.100	29.99	0.947	0.029	1.7

Table 7: Comparison of one-round training and progressive training on *Wineholder*.

Method	PSNR↑	SSIM↑	LPIPS↓
One-round	29.77	0.946	0.033
Progressive	**32.04**	**0.965**	**0.020**

Effect of Early Termination The quantitative results on *Wineholder* of NSVF with early termination with different thresholds are shown in Table 6. The selection of $\epsilon = 0.01$ gives the best trade-off between quality and rendering speed.

Comparion with one round of training at the final resolution As shown in Table 7, our test on *Wineholder* shows that compared with one-round training, our progressive training is faster and easier to train, uses less space and achieves better quality.

C.4 Details for Experiments on ScanNet

We list the details of learning on the ScanNet dataset. We first extract point clouds from all the RGBD images using known camera poses, and register them in the same 3D space. We then initialize a voxel based on the extracted points instead of using a bounding box. No pruning or progressive training are applied in this case. Furthermore, we integrate an additional depth loss based on the provided depth image, that is,

$$\mathcal{L}_{\text{depth}} = \sum_{\boldsymbol{p}_0, \boldsymbol{v}} |Z(\boldsymbol{p}_0, \boldsymbol{v}) - Z^*(\boldsymbol{p}_0, \boldsymbol{v})|_1 \tag{7}$$

where Z^* is the ground truth depth and Z is the expected distance where each ray terminates at this distance in Algorithm 1. We show more qualitative results in Figure 12 and the quantitative comparisons in Table 8 where NSVF achieves the best performance.

Table 8: Quantitative results for *ScanNet (one scene)* (Left) and *Maria Sequence* (Right). Here geometry accuracy is measured by RMSE of ground-truth depths and depths of rendered geometry. Note that no result for NV is reported for *ScanNet* because training failed to converge.

	RMSE↓	PSNR↑	SSIM↑	LPIPS↓		PSNR↑	SSIM↑	LPIPS↓
SRN	14.764	18.25	0.592	0.586	SRN	29.12	0.969	0.036
NeRF	0.681	22.99	0.620	0.369	NV	33.86	0.979	0.027
Ours (w/o depth)	0.210	25.07	0.668	0.315	NeRF	34.19	0.980	0.026
Ours (w/ depth)	**0.079**	**25.48**	**0.688**	**0.301**	Ours	**38.92**	**0.991**	**0.010**

Figure 12: Our sampled results on ScanNet of two different rooms. From left to right: the predicted image, the initial voxels from the point clouds, and the predicted geometry normals.
.

C.5 Details for Experiments on Maria Sequence

We present additional details for learning on the Maria sequence. The Maria sequence consists of 200 frames of different poses if the same character. Since there exists strong correlation from frame to frame, we model all frames with the same set of initial voxels (a bounding box covers all 200 frames) and utilize a hypernetwork described in (Sitzmann et al., 2019b) to output the weights of the MLPs with the frame index as inputs. We also conduct quantitative comparisons on testing views, and report scores in Table 8. NSVF significantly outperforms all the baseline approaches.

C.6 Procedure for Scene Editing and Composition

The learnt NSVF representations can be readily used for editing and composition. We show the basic procedure to edit a real scene in the following three steps: (1) learn and extract sparse voxels with multi-view 2D input images; (2) apply editing (e.g. translation, cloning, removal, etc.) on the voxels; (3) read the modified voxels and render new images. We illustrate the procedure in Figure 13. Furthermore, by learning the model with multiple objects, we can easily render composed scenes by rearranging learned voxels and rendering at the same time.
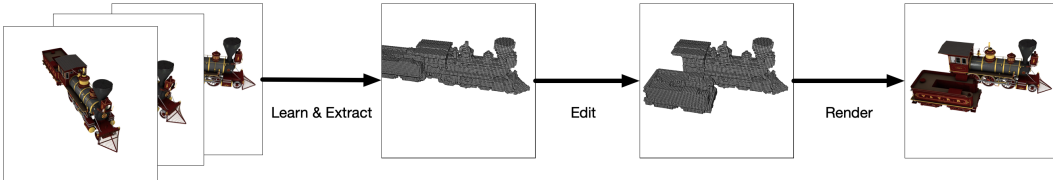

Figure 13: Illustration of scene editing and rendering with NSVF.

D Limitations and Future Work

Although NSVF can efficiently generate high-quality novel views and significantly outperform existing methods, there are four major limitations:

(i) Our method cannot handle scenes with complex background. We assume a simple constant background term (c_{bg}). However, real scenes usually have different backgrounds when viewed from

different points. This makes it challenging to capture their effects correctly without the interference on the learning of the target scenes.

(ii) We set the threshold for self-pruning to be 0.5 in all the experiments. Although this works well for general scenes, incorrect pruning may occur for very thin structures if the threshold is not set properly.

(iii) Similar to Sitzmann et al. (2019b); Mildenhall et al. (2020), NSVF learns the color and density as a "black-box" function of the query point location and the camera-ray direction. Therefore, the rendering performance

Figure 14: A comparison between NSVF output (left) and the groud-truth (right) of a cropped view sampled from scene *lifestyle* (*Synthetic-NSVF* dataset).

highly depends on the distribution of training images, and may produce severe artifacts when the training data is insufficient or biased for predicting complex geometry, materials and lighting effects (see Figure 14 where the refraction on the glass bottle is not learnt correctly). A possible future direction is to incorporate the traditional radiance and rendering equation as a physical inductive bias into the neural rendering framework. This can potentially improve the robustness and generalization of the neural network models.

(iv) The current learning paradigm requires known camera poses as inputs to initialize rays and their direction. For real world images, there is currently no mechanism to handle unavoidable errors in camera calibration. When our target data consists of single-view images of multiple objects, it is even more difficult to obtain accurately registered poses in real applications. A promising avenue for future research would be to use unsupervised techniques such as GANs (Nguyen-Phuoc et al., 2019) to simultaneously predict camera poses for high-quality free-viewpoint rendering results.